Label-free biosensing with a multi-box sub-wavelength phase-shifted Bragg grating waveguide

ENXIAO LUAN,[1,*] ⓘ HAN YUN,[1] ⓘ MINGLEI MA,[1] ⓘ DANIEL M. RATNER,[2] KAREN C. CHEUNG,[1] AND LUKAS CHROSTOWSKI[1]

[1]*Department of Electrical and Computer Engineering, The University of British Columbia, 2332 Main Mall, Vancouver, BC, V6T 1Z4, Canada*
[2]*Department of Bioengineering, University of Washington, 3720 15th Ave NE Seattle, WA 98195-5061, USA*
[*]eluan@ece.ubc.ca

Abstract: Sub-wavelength grating (SWG) metamaterials have been considered to provide promising solutions in the development of next-generation photonic integrated circuits. In recent years, increasied interest has been paid to silicon photonic planar biosensors based on SWG geometries for performance enhancement. In this work, we demonstrate a highly sensitive label-free phase-shifted Bragg grating (PSBG) sensing configuration, which consists of sub-wavelength block arrays in both propagation and transverse directions. By introducing salt serial dilutions and electrostatic polymers assays, bulk and surface sensitivities of the proposed sensor are characterized, obtaining measured results up to 579.2 nm/RIU and 1914 pm/nm, respectively. Moreover, the proposed multi-box PSBG sensor presents an improved quality factor as high as ~8000, roughly 3-fold of the microring-based counterpart, which further improves the detection limit. At last, by employing a biotin-streptavidin affinity assay, the capability for small molecule monitoring is exemplified with a minimum detectable concentration of biotin down to 2.28×10^{-8} M.

1. Introduction

Fluorescence, chemiluminescence, nanoparticles, and enzymatic markers are usually utilized as the label attached to the molecule of interest in biomolecular assays [1]. By the specific confirmation of the label, indirect detection through secondary amplification can be achieved, providing an ultra-high sensitivity. Whereas label detection requires additional tag processing steps, which increases the complexity and cost of detection, more importantly, it potentially alters the intrinsic properties of the target molecules [2]. Label-free detection has been regarded as a promising analytical tool for biomolecular kinetic binding analysis since the pioneering label-free investigation based on surface plasmon resonance (SPR) by Biacore Pharmacia in 1990 [3]. In contrast with label methods, label-free detection employs the transducer to directly monitor essential properties of the target analyte, which significantly reduces the time and effort for each assay and eliminates experimental uncertainty induced by the artificial label probe [4]. Furthermore, label-free methods can be applied for real-time kinetic monitoring and rapid quantification since they offer more direct information with native proteins and ligands in action [2].

Silicon photonic devices using silicon-on-insulator (SOI) platforms have shown promise as optical sensors for label-free diagnostics over the past few decades. Their compatibility with complementary metal-oxide semiconductor (CMOS) foundries, and high refractive index contrast between the silicon core and surrounding medium enable miniaturized compact sensing devices on a single chip with low cost and high yield [3,5]. In addition, CMOS fabrication also provides the possibility to integrate the light source, the transducer, and readout components

on a single substrate as a portable lab-on-a-chip system, which is in line with the contemporary needs of the point-of-care (POC) and home healthcare diagnostics. It is worth noticing that single binding events monitoring has been proposed by silicon photonic sensors through optical trapping of nanoscale analytes [6], which allows one to accurately locate the target molecule and its internal dynamics with a low sample consumption. Many evanescent field-based silicon photonic devices have been investigated for label-free biosensing, such as Young's interferometers (YI) [7], Mach-Zehnder interferometers (MZI) [8], microring resonators (MRR) [9], microdisk resonators [10], Bragg gratings (BG) [11], and photonic crystals (PhC) [12]. A lower detection limit, with high and steady sensitivities, is still desired to meet the ever-increasing modern clinical diagnostic demands [13]. Instead of the conventional waveguide, slot-waveguide-based configurations have been developed to enhance sensor performance [14,15]. By increasing the overlap of the evanescent field and analyte within the slot gap, slot-waveguide-based resonator sensors achieve a bulk sensitivity up to 490 nm/RIU [16] and 298 nm/RIU [17] for gas and liquid detection, respectively. However, due to the highly condensed optical mode inside the gap, slot-waveguide-based sensors show less robust to variation of molecule locations, which may yield inaccurate or inconsistent sensing results for low analyte concentrations [18].

Sub-wavelength grating (SWG) waveguides have been considered as an appealing metamaterial since the first demonstrations by the National Research Council of Canada (NRC) in 2006 [19]. By periodically interleaving the silicon core with low index materials, an SWG waveguide is formed with a period (Λ) far smaller than the wavelength (λ) of the light, i.e., $\Lambda \ll \lambda/(2n_{\text{eff}})$, where n_{eff} is the effective index of the proposed waveguide. The SWG waveguide supports a near-lossless optical mode, the Floquet-Bloch (FB) mode, in which reflection and diffraction effects are suppressed [20]. It has been theoretically [21,22] and experimentally [23] demonstrated that SWG-based planar sensing resonators have enhanced performance, with a high bulk sensitivity (S_{bulk}) of over 400 nm/RIU (nanometer per refractive index unit), due to the optical evanescent field being significantly expanded as compared to a solid core waveguide. Recently, we have investigated a performance-improved SWG biosensor by utilizing a multi-box structure, where the periodicity is not only in the propagation direction but also in the transverse direction [24]. Compared to traditional SWG waveguides, multi-box waveguides support an even less confined optical mode, and have more surface area around each silicon segment for analyte attachment, since the multi-box structure can be seen as a combination of an SWG waveguide with a multi-slot waveguide, both approaches provide increased interaction with the analyte. The MRR based on the multi-box waveguide has a S_{bulk} of 580 nm/RIU, nearly 20% higher than the typical SWG sensor [24]. However, in terms of the detection limit (DL), multi-box waveguide-based MRR sensors exhibit unsatisfactory performance as a result of the relatively high optical losses, which induces a low quality factor (Q-factor). It has been proven that a high Q-factor can prolong the light-matter interaction time and reduce the signal noise, thus improving the detection limit (DL = 3σ/S, where σ is the standard deviation of the noise, and S is the sensitivity) [25]. Therefore, the Q-factor is regarded as another important figure of merit in the development of resonator-based sensors.

In this article, we follow up on the investigation of multi-box structures for high-performance biosensing applications. Instead of employing the MRR, we introduce a phase-shifted Bragg grating (PSBG) resonator consisting of multi-box silicon segments (presented in Fig. 1), which does not suffer from bend radiation losses and presents a smaller footprint [26]. As shown in the insets of Fig. 1, compared to the conventional waveguide, multi-box waveguides enable more light-matter interactions between silicon segments, where there is a large electric field. By optimizing the stop band and central resonant peak size of the proposed multi-box PSBG, an improve Q-factor as high as ~8000 is achieved with water cladding in the quasi-transverse electric (TE) mode, over two times higher than the multi-box MRR sensor (~2600) [24]. Sensor performances regarding bulk and surface sensitivities are characterized by introducing salt

dilutions and electrostatic polymers assays, achieving bulk and surface sensitivities of 579.2 nm/RIU and 1941 pm/nm, respectively. Furthermore, a small molecule interaction test using the biotin-streptavidin affinity model is carried out. By tracking the wavelength shift of the resonant peak, a detection limit of biotin on the order of 10^{-8} molar (M) is observed, indicating the promising potential of silicon photonic planar biosensors for real-time monitoring of small molecule (molecular weight, MW ≤ 1000 Da) interactions.
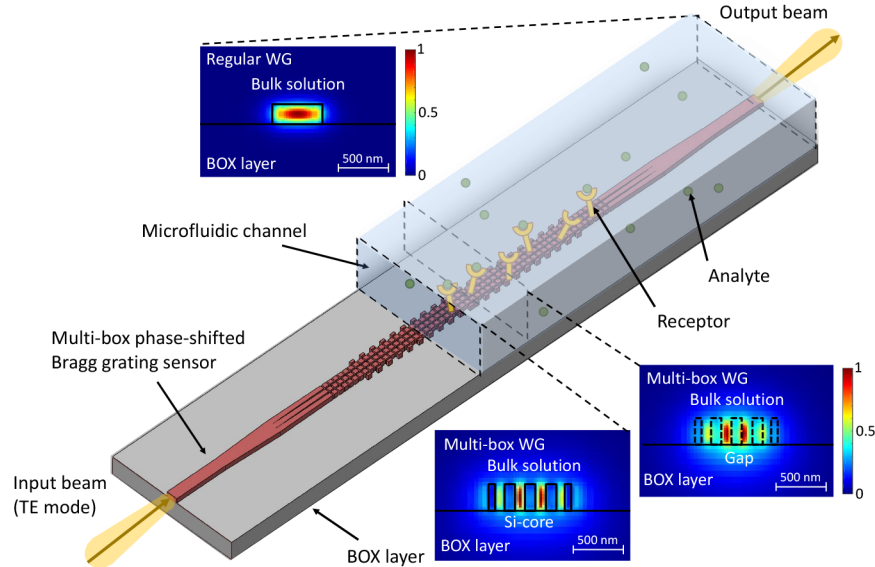

Fig. 1. Schematic of the proposed multi-box phase-shifted Bragg grating (PSBG) sensor integrated with a microfluidic channel in which molecule interactions happen at the sensor surface, leading to a change in the waveguide's effective index. Insets: Cross-sections of electric field distributions in conventional (top left) and multi-box (bottom right, including the distribution in silicon segments and gaps) waveguides, respectively, in the quasi-transverse electric (TE) mode.

2. Design and modelling

2.1. Phase-shifted Bragg gratings

A Bragg grating waveguide is a structure with a periodic modulation of the effective index in the propagation direction, realized by varying the refractive index (RI) of materials or physical waveguide dimensions [27]. Due to the periodic reflections from index changes, a strong reflected signal occurs as a stop band around one particular wavelength, namely the Bragg wavelength. At other wavelengths, light is transmitted through the grating. In terms of biosensing, a phase-shifted cavity is typically introduced in the middle of the grating, forming a first-order Fabry-Perot (FP) cavity between two Bragg reflectors [28]. Different from a uniform Bragg grating, a resonant transmission peak appears within the stop band, presenting a narrow Lorentzian line shape [27], which can be utilized for RI monitoring.

Although there are SWG-based Bragg gratings investigations in the field of optical communications [29,30], to the best of our knowledge, no such devices have been reported for sensing. Figure 2 below illustrates the schematic of the multi-box Bragg grating device with a phase-shifted cavity at the center. Two periods exist in this configuration: one is the period of Bragg gratings (Λ_1); the other is the period of the multi-box SWG ($\Lambda_2 = \Lambda_1/2$). RI modulation for the Bragg grating is achieved by periodically adding corrugation boxes parallel to the main

waveguide, with a corrugation width of ΔW. The length of each corrugation box is the same as the silicon box (L_{Si}) inside the main waveguide, which equals $\eta \times \Lambda_2$ (η is the duty cycle of the multi-box SWG). On each side of the phase-shifted cavity, the Bragg unit is replicated N times as the reflector. According to the previous study, we have found that the length of each silicon box should be not less than 180 nm with a gap of 60 nm, to minimize the optical leakage into the substrate [24]. Measurements indicate that the propagation losses in a multi-box waveguide are mainly generated from the cladding material absorption and sidewall roughness scattering [31]. Although a wider multi-box waveguide (more rows in the main waveguide) shows an improved sensitivity compared to the narrower one, it suffers more optical losses from water absorption and sidewall scattering due to the delocalized optical mode and multiplied sidewalls. Therefore, we select multi-box waveguides with 3, 4, and 5 rows for further analysis.
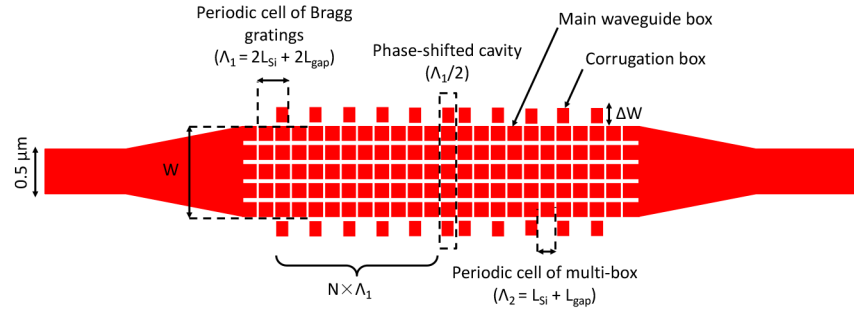

Fig. 2. Two-dimensional schematic geometry of a 5-row multi-box PSBG waveguide with a thickness of 220 nm (Λ_1 and Λ_2 are the period of Bragg gratings and multi-box blocks, L_{Si} and L_{gap} are the length of silicon boxes and gaps in between, W and ΔW are the width of the main waveguide and corrugation boxes, and N is the number of periods on each side).

2.2. Configuration modelling

The stop band and resonant peak in the transmission spectrum can be optimized by adjusting various grating parameters through design. Simulations of multi-box Bragg gratings were realized by employing Bloch boundary conditions on a single grating periodic cell (as shown in Fig. 2) using a fully vectorized three-dimensional Finite-Difference-Time-Domain (3D-FDTD) approach, similar to Ref. [32], which was originally applied for band structure calculations of photonic crystals [33]. By sweeping the length of the silicon box (L_{Si} = 180–200 nm) but keeping the gap distance constant (L_{gap} = 60 nm), the effect of Bragg period (Λ_1 = 2($L_{Si} + L_{gap}$) = 480–520 nm) on the central wavelength position of the stop band is shown in Fig. 3(a) with the width of corrugation boxes fixed (ΔW = 120 nm). All band structure calculations assume that the periodic cell is infinitely repeated ($N = \infty$).

We used a coupled-mode-theory-based transfer matrix method (CMT-TMM) to calculate the spectral responses of proposed multi-box PSBGs with various geometrical parameters. The transmission and reflection responses can be calculated using [34]:

$$\begin{bmatrix} A_{in} \\ B_{in} \end{bmatrix} = GPG \begin{bmatrix} A_{out} \\ B_{out} \end{bmatrix} = \begin{bmatrix} M_{11} & M_{12} \\ M_{21} & M_{22} \end{bmatrix} \begin{bmatrix} A_{out} \\ B_{out} \end{bmatrix}, \tag{1}$$

where A and B are the electric fields of the forward and backward propagating modes at the input and output of the device, respectively, G represents the transfer matrices of the grating on each side, and P represents the matrix of the phase-shifted cavity in the middle. The analytic solution
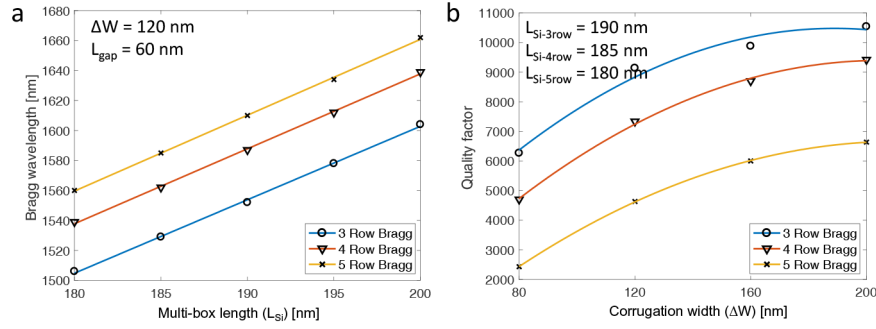
Fig. 3. (a) Simulated central wavelengths of the stop band as a function of the length of multi-box blocks (L_{Si}) for 3, 4, and 5-row multi-box Bragg gratings (ΔW = 120 nm, and L_{gap} = 60 nm). (b) Simulated Q-factors from the transmission spectra versus the variation of the corrugation width of 3, 4, and 5-row multi-box Bragg gratings ($L_{Si\text{-}3row}$ = 190 nm, $L_{Si\text{-}4row}$ = 185 nm, and $L_{Si\text{-}5row}$ = 180 nm).

for the matrix G can be obtained by treating it as a uniform grating:

$$G = \begin{bmatrix} cosh(sL_G) + j\frac{\Delta\beta'}{2s}sinh(sL_G) & j\frac{\kappa}{s}sinh(sL_G) \\ -j\frac{\kappa}{s}sinh(sL_G) & cosh(sL_G) - j\frac{\Delta\beta'}{2s}sinh(sL_G) \end{bmatrix},$$ (2)

where $s = \sqrt{\kappa^2 - (\Delta\beta'/2)^2}$, $\Delta\beta' = 2\beta' - 2\pi/\Lambda$, and $\beta' = \beta - j\alpha/2$. Among them, β is the propagation constant in the grating, Λ is the period of Bragg, L_G is the length of the grating mirror on each side, κ is the coupling coefficient, and α is the propagation loss per length, respectively. For the phase-shifted cavity, the central matrix P is given by:

$$P = \begin{bmatrix} e^{j\beta'L_P} & 0 \\ 0 & e^{-j\beta'L_P} \end{bmatrix},$$ (3)

where L_P is the length of the central phase-shifted cavity. Therefore, the transmission spectrum of the through-port is given by $T = 1/|M_{11}|^2$.

We chose the silicon box length of 190, 185, and 180 nm for 3, 4, and 5-row multi-box Bragg gratings, respectively, and evaluated the Q-factor of each PSBG configuration as a function of the corrugation width. The aforementioned FDTD-based band structure approach was used to obtain the n_{eff}, n_g, and stop band bandwidth ($\Delta\lambda_{PSBG}$) of the proposed device. The propagation constant β of the excited Bloch mode in the grating was calculated through $\beta = 2\pi n_{eff}/\lambda$. The coupling coefficient κ can be extracted by [35]:

$$\kappa = \frac{\pi n_g \Delta\lambda_{PSBG}}{\lambda_c^2},$$ (4)

where λ_c is the central wavelength of $\Delta\lambda_{PSBG}$. The propagation losses α of 3, 4, and 5-row multi-box waveguides (with no corrugations) were approximately 34, 41, and 48 dB/cm, respectively, which were based on our previous measurements in water [31]. By bringing β, κ, and α into the above formulas, a transmission spectrum was acquired for each PSBG, where $L_G = N \times \Lambda_1 = 140\Lambda_1$ and $L_P = \Lambda_1/2$ (defined as the quarter-wave PSBG). Simulated Q-factors were extracted directly from transmission spectra ($Q \approx \lambda_{res}/\Delta\lambda_{FWHM}$, where λ_{res} is the resonant wavelength, and $\Delta\lambda_{FWHM}$ is the full width at half maximum of the resonant peak) and plotted in Fig. 3(b). By enlarging ΔW from 80 to 200 nm, a growing Q-factor value is observed, which results from the

increased κ and decreased mirror loss (α_{mirror}). However, it is important to note that Q-factor is ultimately limited by the waveguide loss (α_{wg}); in other words, the maximum transmission is not unity due to the loss, which determines the extinction ratio (ER) of the resonant peak [27].

3. Experiments and results

3.1. Device fabrication

Silicon photonic devices were designed using the open-source GDS editor KLayout and a publicly accessible open-source Process Design Kit (SiEPIC-EBeam-PDK) [36], and fabricated on the SOI wafer with 220-nm-thick silicon and 2-μm-thick buried oxide (BOX) layers (SOITec, Grenoble, France) through the NanoSOI Multi-Project Wafer (MPW) fabrication process by Applied Nanotools Inc., (Edmonton, Canada). The patterns were defined in negative-tone hydrogen silsesquioxane (HSQ) e-beam resist by direct-write 100 keV electron-beam lithography system (EBL, JEOL JBX-81OOFS), and transferred into the silicon by the inductively coupled plasma reactive-ion etching (ICP-RIE) process, with a minimum feature size of 60 nm. Devices were then exposed to air for further biosensing investigations.

3.2. Experimental instrumentation

Optical measurements and biosensing characterization were carried out by using a custom silicon photonic test setup and software controlled by a Windows PC. A tunable laser (Agilent 81600B, 1480–1620 nm) and power detectors (Agilent 81635A) were employed as the optical source and readout. A four-port polarization maintaining fiber-array (PLC Connections, Columbus, OH) was connected to the lightwave mainframe to couple the light on and off the silicon chip. A 6-mm-thick poly(methyl methacrylate) (PMMA)/polydimethylsiloxane (PDMS, SYLGARD 184, Dow Corning) gasket with two parallel microfluidic channels was aligned and fixed to the chip on an aluminum stage, which was thermally tuned by a temperature controller (LDC501, Stanford Research Systems). A syringe pump (Chemiyx Nexus 3000) was used to sequence the reagents through the channels in withdrawal mode. A Matlab-based program was employed to fit the spectra with a smoothing-spline interpolation function to track the resonant peak movement.

To evaluate the ER and Q-factor, multi-box PSBGs were designed and fabricated with varied ΔW and N. Figure 4(a) shows measured ERs and Q-factors with different ΔW values of 3, 4, and 5-row PSBG waveguides. Other parameters were based on simulations presented in Fig. 3: for 3-row PSBGs, $N = 140$, $\Lambda_2 = 250$ nm, and $\eta = 76\%$; for 4-row PSBGs, $N = 140$, $\Lambda_2 = 245$ nm, and $\eta = 75.5\%$; for 5-row PSBGs, $N = 140$, $\Lambda_2 = 240$ nm, and $\eta = 75\%$. In Fig. 4(b), the effect of N is evaluated, where the corrugation width is 120, 140, and 160 nm for 3, 4, 5-row PSBGs, respectively. Measurement results indicate that the Q-factor increases with the increase of ΔW and N and reaches a plateau, which is eventually dominated by α_{wg}. For the ER value, it achieves a maximum under the critical coupling condition but starts to reduce as N continues to grow, due to the high intensity loss in long devices. A suppressed ER may push the resonant peak into the noise and lead to a low signal-to-noise ratio (SNR) for optical powers. To achieve a high Q-factor while maintaining an acceptable ER for sensing assessments, 3, 4, and 5-row multi-box PSBG waveguide-based sensors were selected according to following parameters: for 3-row PSBGs, $N = 140$, $\Delta W = 120$ nm, and $L_{\text{Si}} = 190$ nm; for 4-row PSBGs, $N = 160$, $\Delta W = 140$ nm, and $L_{\text{Si}} = 185$ nm; for 5-row PSBGs, $N = 160$, $\Delta W = 160$ nm, and $L_{\text{Si}} = 180$ nm. The gap between silicon blocks (L_{gap}) equals the minimum feature size of 60 nm in all configurations.

3.3. Sensitivity characterization

Bulk and surface sensitivities are two metrics used for evaluating sensor performance of evanescent field-based optical sensors, which take into account RI changes of the entire cladding (S_{bulk}) and within the first few tens to hundreds of nanometers above the waveguide (S_{surf}), respectively
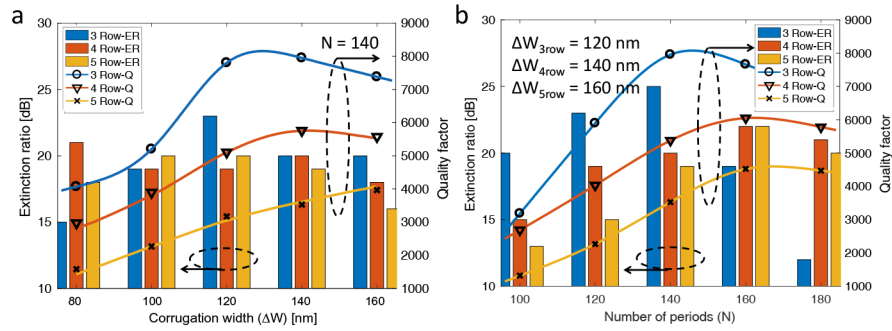
Fig. 4. (a) Measured extinction ratio (ER, in the bar chart) and quality factor (*Q*-factor, in the curve graph) values as a function of the corrugation width (ΔW) in 3, 4, and 5-row PSBG waveguides. Fixed parameters: $N = 140$, $L_{Si\text{-}3row} = 190$ nm, $L_{Si\text{-}4row} = 185$ nm, and $L_{Si\text{-}5row} = 180$ nm. (b) Measured ER and *Q*-factor values as a function of the number of periods (*N*) in 3, 4, and 5-row PSBG waveguides. Fixed parameters: $\Delta W_{3row} = 120$ nm, $\Delta W_{4row} = 140$ nm, and $\Delta W_{5row} = 160$ nm. For the 3-row PSBG with N = 180, the *Q*-factor is not included due to the noisy resonant behavior caused by the low ER.

[35]. To characterize the sensing capability of the proposed multi-box PSBG device, two typical bioassays, sodium chloride (NaCl) RI titrations and electrostatic polymer binding were investigated, which have been applied to evaluate the bulk RI change sensitivity and surface evanescent field profile of MRR sensors [37,38]. To have a performance comparison between 3, 4, and 5-row multi-box PSBG sensors, a test structure consisting one input port (on-chip grating coupler) and three output ports was designed and fabricated (Fig. 5(a)), where the input light is split into three PSBG waveguides by two standard Y-branches. Figure 5(b) shows the measured transmission spectra of the proposed test structure after calibration, presenting a measured *Q*-factor of 7800, 6100, and 4600 for 3 (blue curve), 4 (red curve), and 5-row (yellow curve) PSBG sensors, respectively. The resolution of the tunable laser was set to 10 pm for the wavelength sweep, which reduces the scan interval to 30 s for a 50-nm sweep. To improve the resolution of the measurement result, an optical spectrum curve fitting method, the smoothing-spline interpolation function with a smoothing parameter of 0.9999, was employed to obtain an enhanced resolution of 0.1 pm (as shown in the inset of Fig. 5(b)), which can effectively reduce the measurement noise [39].

The bulk sensitivity was assessed by injecting NaCl dilutions ranging from 62.5 to 500 mM through sensing devices with a flow rate of 20 µL/min. To minimize the external noise caused by the thermal drift, the stage was thermally tuned to 25°C during the measurement. As shown in Fig. 5(c), the sensorgrams of 3, 4, and 5-row multi-box PSBGs present stepped wavelength shifts as a function of the concentration of NaCl, leading to a bulk sensitivity of 551.2, 567.5, and 579.2 nm/RIU, respectively (Fig. 5(d)). Experiments were repeated multiple times to ensure signal accuracy and stability. To further determine the detection limit of proposed sensors, the system noise floor, which includes the thermal drift, light source fluctuation and detector noise, was evaluated by constantly introducing deionized (DI) water to sensors for 3 hours, obtaining the three standard deviations (3σ) of 2.3, 3.0, and 3.4 pm, respectively. Therefore, in terms of bulk sensing, the system DL (sDL) is on the order of 10^{-6} RIU. The sDL depends on the readout instrumentation and the experimental setup, which impedes the objective comparison between sensors under different bio-assays and experimental systems. Another well-established metric, namely the intrinsic DL (iDL = $\lambda/(Q \times S)$), only relies on the intrinsic characteristics of the resonator-based sensor [40]. The lowest iDL of proposed multi-box PSBG sensors is around 3.6 $\times 10^{-4}$ RIU, comparable to the best resonator-based SOI sensors [41].
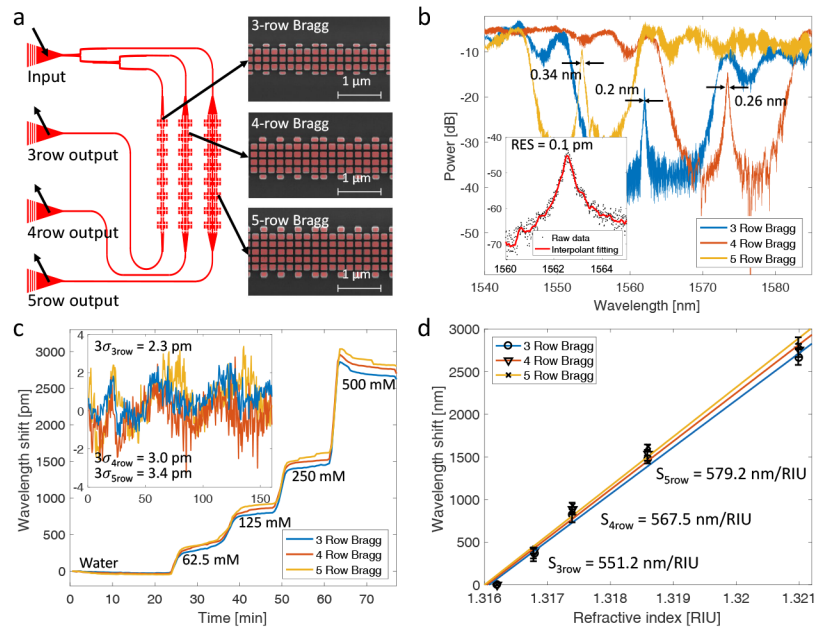
Fig. 5. (a) Schematic of the proposed sensing device with one input and three outputs connecting with 3, 4, and 5-row multi-box PSBGs, as well as the scanning electron microscope (SEM) images, focused at the center of the phase-shifted cavity, where silicon is false-colored. (b) Measured transmission spectra of the proposed device, after calibrated by a similar 4-port device where PSBGs are replaced by standard waveguides. Inset: A closer look at the resonant peak of the 3-row PSBG waveguide before (black dots) and after (red curve) the curve fitting, exhibiting a 100-fold enhanced resolution of 0.1 pm. (c) Wavelength shift sensorgrams of bulk refractive index (RI) steps with NaCl dilutions from 62.5 to 500 mM. Inset: The system noise floor of proposed multi-box PSBG sensors at 25°C. (d) Bulk sensitivity results of 3, 4, and 5-row multi-box PSBGs. Refractive indices of NaCl dilutions were calculated at 1550 nm based on a third-order polynomial fit from Ref. [42].

To investigate the surface sensitivity, a layer-by-layer electrostatic polymer deposition approach was employed based on Ref. [38] by introducing polyethylenimine (PEI), polystyrene sulfonate (PSS), and polyallylamine hydrochloride (PAH) to the sensor surface. All polymers were dissolved in Tris buffer (0.5 mM, pH = 7.4, Sigma-Aldrich) to 5 mg/mL. As illustrated in Fig. 6(a), the sensor chip was first cleaned by a piranha solution (3:1 H_2SO_4:H_2O_2) at 100°C for 10 min, which removes organic pollutants and forms hydroxyl groups on the surface (caution, piranha solution reacts violently with organic solvents). Then, the chip was exposed to positively charged PEI (MW 5000 Da, Sigma-Aldrich) for 5 min to ensure the sufficient coverage of the initial adhesion, and followed by adequate Tris buffer rinse. Next, negatively charged PSS (MW 70000 Da, Sigma-Aldrich) and positively charged PAH (MW 17500 Da, Sigma-Aldrich) were alternated to the surface for 5 min, respectively. A 5-min Tris buffer flushing was performed after each deposition to avoid polymer precipitation and clogging. All solutions were injected with a flow rate of 20 μL/min at 25°C. The layer-by-layer deposition result of polyelectrolytes is presented in Fig. 6(b) as a function of time. The inset of Fig. 6(b) shows a zoom-in view of two successive deposition cycles. To obtain the surface sensitivity of proposed multi-box PSBG sensors, the thickness of the bilayer is required. Glass slides with 5, 10, and 15 bilayers were manually prepared by using the same polyelectrolytes, and measured through a thin-film measurement system (Filmetrics F20-UVX) with an assumption of $n_{polymer} = 1.50$ at 1550 nm wavelengths.

Measurements indicate a thickness of 1.987 nm per PSS/PAH bilayer depicted in the inset of Fig. 6(c). Surface sensitivities of multi-box PSBGs are presented in Fig. 6(c) with a highest S_{surf} of 1941 pm/nm, in good agreement with previous experiments [31].
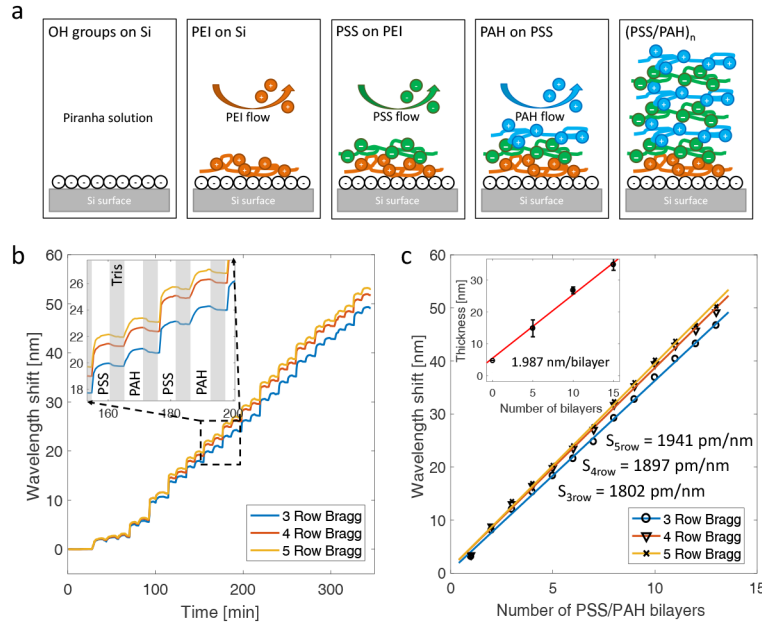

Fig. 6. (a) Schematic of the layer-by-layer polyelectrolytes deposition process at the surface of proposed sensors. (b) Measured wavelength shifts of 3, 4, and 5-row multi-box PSBGs in terms of the deposition of polymers. Inset: An amplification of the wavelength shift in two deposition cycles: a more substantial shift (2 nm) is observed in PSS than in PAH (1 nm) due to the molecular weight (MW) difference. (c) Surface sensitivities of proposed sensors. Inset: Measured thicknesses of different numbers of PSS/PAH bilayers on the glass slide.

3.4. Detection of small molecules

Real-time measurements of protein molecule interactions are of great importance for both fundamental research and biomedical applications. Due to the large variety of chemical compounds from natural or pharmaceutical sources, the detection and quantification of small molecules (typically less than 1000 Da in size) have attracted much attention in a wide range of fields [43]. Surface plasmon resonance (SPR) has been demonstrated as one of the most powerful technologies to determine specificity, affinity and kinetic parameters for label-free protein-protein binding analysis [44]. Due to the increasing demand for modern drug discovery approaches, the development of high-performance SPR technology is further accelerated, prompting SPR as a validated tool for monitoring small molecule interactions [45]. However, SPR-based approaches usually require expensive and bulky instruments as well as trained operators, which restricts their broad adoption for the clinical and home health-care diagnosis, especially in developing countries. Consequently, silicon photonic-based planar sensors are regarded as a simplified and disposable alternative. However, the magnitude of the wavelength shift or intensity change for an evanescent field-based sensor is linearly proportional to the mass change due to the adsorption at the surface, it is challenging for the conventional waveguide-based silicon photonic sensor to detect analytes with small MWs, typically at low concentrations.

To explore the small molecule monitoring capability of the proposed sensor, we applied the well-studied biotin-streptavidin model to the 3-row PSBG sensing device. Biotin is a water-soluble B-vitamin with a very small MW of 244 Da. It has the strongest known non-covalent protein-ligand interaction with the tetrameric protein avidin (also streptavidin and neutravidin), showing a dissociation constant (K_d) of 10^{-15} M in solution [46]. Instead of the multi-cycle kinetics (MCK) assay which is commonly used in SPR detection, the kinetic titration series (or single-cycle kinetics, SCK) approach was employed in this work [47]. Different from the classic MCK requiring complete analyte removal between measurement cycles, SCK involves sequentially injecting an analyte concentration series without any regeneration steps, which provides binding constants as precise as the MCK method of analyte injections [48].

In comparison with direct adsorption, proteins attached via chemical links at the sensor surface are in their natural globular conformations and provide high activity [49]. Therefore, as depicted in Fig. 7(a), the sensor surface was functionalized through a chemical linking method: after cleaning with the piranha solution, the chip was first exposed to phosphate buffered saline (PBS, pH = 7.4, Gibco) to obtain a stable baseline; then, a high concentration (150 µg/mL) of biotinylated Bovine Serum Albumin (bBSA, MW ~66 kDa, Vector Labs) was introduced to the surface as a crosslinker (Step A), and incubated for 1 h for a near-maximum coverage; after coating with bBSA, 50 µg/mL streptavidin (SA, MW ~57 kDa, Vector Labs) was followed up for the surface modification via the biotin-SA linkage (Step B); at last, the chip was subjected to 50 µg/mL Bovine Serum Albumin (BSA, MW ~66 kDa, Sigma-Aldrich) to block any remaining exposed surface sites (Step C). Each step was followed by copious PBS buffer rinse to remove any unbound molecule on the surface. After the attachment of bio-receptors, a set of biotin dilutions with concentrations of 10^{-11}, 10^{-9}, 10^{-7}, 10^{-5}, and 10^{-3} M were injected over the sensor sequentially (Step D). The association and dissociation times were set to 5 min and 3 min, respectively, with a flow rate of 30 µL/min for each concentration. All steps were performed at 25°C. In addition, a control experiment was performed in parallel to quantify the specific binding between biotin and SA molecules, where all the surface modification steps were the same except that SA was replaced by BSA in Step B. The sensorgrams of surface modification and SCK assay are shown in Fig. 7(b), presenting the time-dependent wavelength shift for both sensing and control experiments.

The wavelength shift of the biotin-SA interaction is depicted in Fig. 7(c), presenting saw-tooth like patterns after baseline detrending. For the sensing data (blue curve), the resonant peak shows 0.08, 1.51, 7.02, 10.05, and 10.97 pm shifts for each concentration of biotin dilutions. As for the reference data (red curve), there is no noticeable shift larger than the $3\sigma_{3\text{row}}$ of the systematic noise after PBS rinsing, indicating a negligible non-specific binding between biotin and BSA. The analyte binding capacity of the sensing surface depends on the density of available binding sites from immobilized receptors. The theoretical maximum binding response R_{max} of the analyte is determined by [50]:

$$R_{max} = \frac{M_{analyte}}{M_{receptor}} R_{ads} \times n \tag{5}$$

where $M_{analyte}$ and $M_{receptor}$ are MW values of the analyte and receptor, respectively, R_{ads} is the sensor response of the immobilization of receptors at the surface, and n is the molar ratio of the binding sites in the receptor. Due to the surface immobilization of the SA capture protein, it is predicted that two ($n = 2$) of the four potential biotin-binding sites on SA will be available for subsequent interactions with soluble biotin [51]. The adsorption of 50 µg/mL SA (Step B) presented an observed resonant wavelength shift of $R_{ads} = 1.33$ nm following the buffer rinse (Fig. 7(b)). Based on Eq. 5, the device's theoretical R_{max} of the biotin-SA interaction for two binding sites is 11.39 pm, remarkably close to the observed value of 10.97 pm.

The resonant wavelength shift as a function of the concentration of biotin is plotted in Fig. 7(d), and fitted with the Langmuir equation $\Delta\lambda/\Delta\lambda_{max} = c/(K_d + c)$, where $\Delta\lambda$ is the wavelength shift
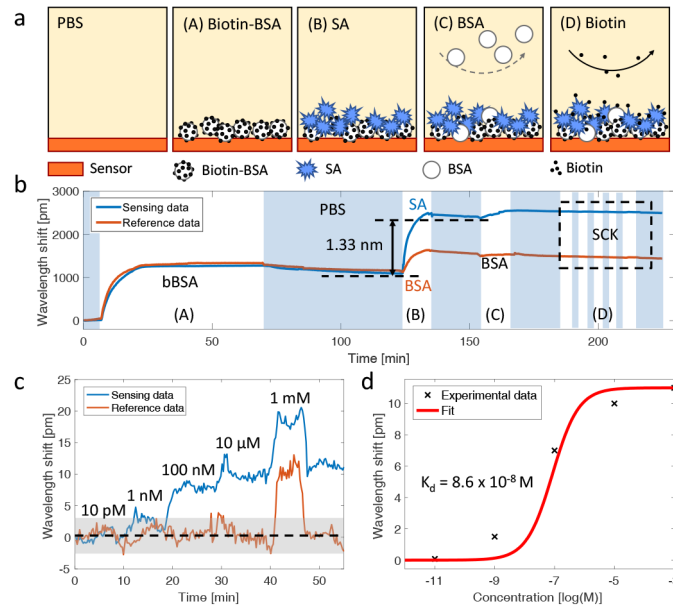
Fig. 7. (a) Schematic of the surface functionalization and biotin titrations steps: Step A = 150 µg/mL biotinylated Bovine Serum Albumin (bBSA), Step B = 50 µg/mL streptavidin (SA), Step C = 50 µg/mL Bovine Serum Albumin (BSA), and Step D = biotin dilutions. Each step was washed with sufficient PBS buffer. (b) Complete sensorgrams of the small molecule interaction assay, where the blue curve represents the experimental (sensing) data, and the red curve represents the control (reference) data. Light blue portions indicate PSB rinsing steps. (c) Zoomed sensorgrams of single-cycle kinetic (SCK) titrations using biotin dilution series at concentrations of 10^{-11}, 10^{-9}, 10^{-7}, 10^{-5}, and 10^{-3} M. Each concentration was injected with a flow rate of 30 µL/min for 5 min and followed with a 3-min PBS rinse. The grey area shows the 3σ of the system noise. (d) Wavelength shift as a function of the concentration of biotin, which is fitted with the Langmuir equation, indicating a dissociation constant (K_d) of 8.6×10^{-8} M.

for each concentration, $\Delta\lambda_{max}$ is the shift corresponding to the saturation of binding sites, and c is the analyte concentration. If we assume a maximum binding site occupation happens at the concentration of 10^{-3} M (i.e., $\Delta\lambda_{max} = 10.97$ pm), the dissociation constant estimated from fitting is 8.6×10^{-8} M, larger than the free solution-based affinity value ($K_d = 10^{-15}$ M). Multiple publications have reported the same discrepancy between the binding kinetics of surface-capture vs. solution-phase SA-biotin interactions. This has been theorized to be due to mass transport limitations, altered diffusional characteristics, multivalent binding, and ligand alteration due to the immobilization of SA to a solid substrate [52–54]. By employing the measured $3\sigma_{3row}$ in the fitting equation, a minimum detectable biotin concentration of 2.28×10^{-8} M is obtained, 17-fold lower than a home-made SPR-based analytical system [55].

4. Conclusion

We propose and experimentally demonstrate an optical sensing configuration based on phase-shifted Bragg gratings by using multi-box waveguides in the TE mode. Compared to MRR-based counterparts, multi-box PSBG sensors have similar bulk and surface sensitivities but exhibit an improved Q-factor and a smaller footprint ($\sim 200\ \mu m^2$). Owing to no bend radiation losses, the proposed multi-box PSBG sensor presents higher Q-factors around 8000 at 1550 nm wavelengths, leading to an intrinsic DL of 3.6×10^{-4} RIU, which is close to half of that of the well-investigated

MRR sensor in the TM mode (7.1×10^{-4} RIU). Moreover, because of the highly expanded surface contact area, the multi-box structure is suitable for real-time protein-ligand interaction kinetics monitoring, even for analytes with low MWs. By sequentially introducing biotin dilutions to the streptavidin-modified 3-row PSBG sensor surface, the biotin-SA interaction model is characterized through single-cycle kinetics without regeneration processes. The capability for the detection of biotin dilutions as low as 2.28×10^{-8} M is observed without label attachment, demonstrating the applicability of the proposed multi-box PSBG sensor for detecting small molecules. This may facilitate the development of silicon-based low-cost sensing systems competitive with SPR. However, due to the high noise level (on the order of pm), the experimental result shows a low SNR even in the case of surface saturation. Besides, the immobilized crosslinker on the surface pre-occupies half of the binding sites of the receptor, which cuts down the achievable signal for the analyte binding. Further work will be performed to minimize the system noise floor and investigate other chemical linkers that do not interact with receptor binding sites.

Disclosures

The authors declare that there are no conflicts of interest related to this article.

References

1. A. L. Washburn, L. C. Gunn, and R. C. Bailey, "Label-free quantitation of a cancer biomarker in complex media using silicon photonic microring resonators," Anal. Chem. **81**(22), 9499–9506 (2009).
2. A. Syahir, K. Usui, K.-Y. Tomizaki, K. Kajikawa, and H. Mihara, "Label and label-free detection techniques for protein microarrays," Microarrays **4**(2), 228–244 (2015).
3. L. M. Lechuga, "Optical biosensors," Compr. Anal. Chem. **44**, 209–250 (2005).
4. B. T. Cunningham and L. G. Laing, "Advantages and application of label-free detection assays in drug screening," Expert Opin. Drug Discovery **3**(8), 891–901 (2008).
5. R. Soref, "The past, present, and future of silicon photonics," IEEE J. Sel. Top. Quantum Electron. **12**(6), 1678–1687 (2006).
6. D. Conteduca, C. Reardon, M. G. Scullion, F. Dell'Olio, M. N. Armenise, T. F. Krauss, and C. Ciminelli, "Ultra-high Q/V hybrid cavity for strong light-matter interaction," APL Photonics **2**(8), 086101 (2017).
7. K. Schmitt, B. Schirmer, C. Hoffmann, A. Brandenburg, and P. Meyrueis, "Interferometric biosensor based on planar optical waveguide sensor chips for label-free detection of surface bound bioreactions," Biosens. Bioelectron. **22**(11), 2591–2597 (2007).
8. A. Densmore, M. Vachon, D.-X. Xu, S. Janz, R. Ma, Y.-H. Li, G. Lopinski, A. Delâge, J. Lapointe, C. Luebbert, Q. Liu, P. Chenben, and J. Schmid, "Silicon photonic wire biosensor array for multiplexed real-time and label-free molecular detection," Opt. Lett. **34**(23), 3598–3600 (2009).
9. M. Iqbal, M. A. Gleeson, B. Spaugh, F. Tybor, W. G. Gunn, M. Hochberg, T. Baehr-Jones, R. C. Bailey, and L. C. Gunn, "Label-free biosensor arrays based on silicon ring resonators and high-speed optical scanning instrumentation," IEEE J. Sel. Top. Quantum Electron. **16**(3), 654–661 (2010).
10. S. M. Grist, S. A. Schmidt, J. Flueckiger, V. Donzella, W. Shi, S. T. Fard, J. T. Kirk, D. M. Ratner, K. C. Cheung, and L. Chrostowski, "Silicon photonic micro-disk resonators for label-free biosensing," Opt. Express **21**(7), 7994–8006 (2013).
11. A. Jugessur, J. Dou, J. Aitchison, R. De La Rue, and M. Gnan, "A photonic nano-Bragg grating device integrated with microfluidic channels for bio-sensing applications," Microelectron. Eng. **86**(4-6), 1488–1490 (2009).

12. D. Yang, H. Tian, and Y. Ji, "High-q and high-sensitivity width-modulated photonic crystal single nanobeam air-mode cavity for refractive index sensing," Appl. Opt. **54**(1), 1–5 (2015).

13. M. S. Luchansky, A. L. Washburn, M. S. McClellan, and R. C. Bailey, "Sensitive on-chip detection of a protein biomarker in human serum and plasma over an extended dynamic range using silicon photonic microring resonators and sub-micron beads," Lab Chip **11**(12), 2042–2044 (2011).

14. C. A. Barrios, K. B. Gylfason, B. Sánchez, A. Griol, H. Sohlström, M. Holgado, and R. Casquel, "Slot-waveguide biochemical sensor," Opt. Lett. **32**(21), 3080–3082 (2007).

15. F. Dell'Olio and V. M. Passaro, "Optical sensing by optimized silicon slot waveguides," Opt. Express **15**(8), 4977–4993 (2007).

16. J. T. Robinson, L. Chen, and M. Lipson, "On-chip gas detection in silicon optical microcavities," Opt. Express **16**(6), 4296–4301 (2008).

17. T. Claes, J. G. Molera, K. De Vos, E. Schacht, R. Baets, and P. Bienstman, "Label-free biosensing with a slot-waveguide-based ring resonator in silicon on insulator," IEEE Photonics J. **1**(3), 197–204 (2009).

18. J. R. Bickford, P. S. Cho, M. E. Farrell, E. L. Holthoff, and P. M. Pellegrino, "The investigation of subwavelength grating waveguides for photonic integrated circuit based sensor applications," IEEE J. Sel. Top. Quantum Electron. **25**(3), 1–10 (2019).

19. P. Cheben, D.-X. Xu, S. Janz, and A. Densmore, "Subwavelength waveguide grating for mode conversion and light coupling in integrated optics," Opt. Express **14**(11), 4695–4702 (2006).

20. Z. Weissman and I. Hendel, "Analysis of periodically segmented waveguide mode expanders," J. Lightwave Technol. **13**(10), 2053–2058 (1995).

21. J. G. Wangüemert-Pérez, P. Cheben, A. Ortega-Moñux, C. Alonso-Ramos, D. Pérez-Galacho, R. Halir, I. Molina-Fernández, D.-X. Xu, and J. H. Schmid, "Evanescent field waveguide sensing with subwavelength grating structures in silicon-on-insulator," Opt. Lett. **39**(15), 4442–4445 (2014).

22. V. Donzella, A. Sherwali, J. Flueckiger, S. M. Grist, S. T. Fard, and L. Chrostowski, "Design and fabrication of soi micro-ring resonators based on sub-wavelength grating waveguides," Opt. Express **23**(4), 4791–4803 (2015).

23. J. Flueckiger, S. Schmidt, V. Donzella, A. Sherwali, D. M. Ratner, L. Chrostowski, and K. C. Cheung, "Sub-wavelength grating for enhanced ring resonator biosensor," Opt. Express **24**(14), 15672–15686 (2016).

24. E. Luan, H. Yun, L. Laplatine, Y. Dattner, D. M. Ratner, K. C. Cheung, and L. Chrostowski, "Enhanced sensitivity of subwavelength multibox waveguide microring resonator label-free biosensors," IEEE J. Sel. Top. Quantum Electron. **25**(3), 1–11 (2019).

25. I. M. White and X. Fan, "On the performance quantification of resonant refractive index sensors," Opt. Express **16**(2), 1020–1028 (2008).

26. S. Schmidt, J. Flueckiger, W. Wu, S. M. Grist, S. T. Fard, V. Donzella, P. Khumwan, E. R. Thompson, Q. Wang, P. Kulik, X. Wang, A. Sherwali, J. Kirk, K. Cheung, L. Chrostowski, and D. Ratner, "Improving the performance of silicon photonic rings, disks, and Bragg gratings for use in label-free biosensing," in *Biosensing and Nanomedicine VII*, Vol. 9166 (International Society for Optics and Photonics, 2014), p. 91660M.

27. X. Wang, "Silicon photonic waveguide Bragg gratings", Ph.D. thesis, University of British Columbia (2013).

28. A. Yariv and P. Yeh, "Photonics-optical electronics in modern communication", (2007).

29. J. Wang, I. Glesk, and L. R. Chen, "Subwavelength grating filtering devices," Opt. Express **22**(13), 15335–15345 (2014).

30. J. Čtyroký, J. G. Wangüemert-Pérez, P. Kwiecien, I. Richter, J. Litvik, J. H. Schmid, Í. Molina-Fernández, A. Ortega-Moñux, M. Dado, and P. Cheben, "Design of narrowband Bragg spectral filters in subwavelength grating metamaterial waveguides," Opt. Express **26**(1), 179–194 (2018).

31. E. Luan, H. Yun, L. Laplatine, J. Flückiger, Y. Dattner, D. Ratner, K. Cheung, and L. Chrostowski, "Sub-wavelength multi-box waveguide-based label-free sensors," in *Integrated Optics: Devices, Materials, and Technologies XXII*, Vol. 10535 (International Society for Optics and Photonics, 2018), p. 105350H.

32. X. Wang, Y. Wang, J. Flueckiger, R. Bojko, A. Liu, A. Reid, J. Pond, N. A. Jaeger, and L. Chrostowski, "Precise control of the coupling coefficient through destructive interference in silicon waveguide Bragg gratings," Opt. Lett. **39**(19), 5519–5522 (2014).

33. M. Lončar, T. Doll, J. Vučković, and A. Scherer, "Design and fabrication of silicon photonic crystal optical waveguides," J. Lightwave Technol. **18**(10), 1402–1411 (2000).

34. M. Caverley, X. Wang, K. Murray, N. A. Jaeger, and L. Chrostowski, "Silicon-on-insulator modulators using a quarter-wave phase-shifted Bragg grating," IEEE Photonics Technol. Lett. **27**(22), 2331–2334 (2015).

35. L. Chrostowski and M. Hochberg, *Silicon photonics design: from devices to systems* (Cambridge University Press, 2015).

36. L. Chrostowski, H. Shoman, M. Hammood, H. Yun, J. Jhoja, E. Luan, S. Lin, A. Mistry, D. Witt, N. A. Jaeger, S. Shekhar, H. Jayatilleka, P. Jean, S. B.-d. Villers, J. Cauchon, W. Shi, and C. Horvath, "Silicon photonic circuit design using rapid prototyping foundry process design kits," IEEE J. Sel. Top. Quantum Electron. **25**(5), 1 (2019).

37. L. Laplatine, E. Luan, K. Cheung, D. M. Ratner, Y. Dattner, and L. Chrostowski, "System-level integration of active silicon photonic biosensors using fan-out wafer-level-packaging for low cost and multiplexed point-of-care diagnostic testing," Sens. Actuators, B **273**, 1610–1617 (2018).

38. M. S. Luchansky, A. L. Washburn, T. A. Martin, M. Iqbal, L. C. Gunn, and R. C. Bailey, "Characterization of the evanescent field profile and bound mass sensitivity of a label-free silicon photonic microring resonator biosensing platform," Biosens. Bioelectron. **26**(4), 1283–1291 (2010).
39. J. Hu, X. Sun, A. Agarwal, and L. C. Kimerling, "Design guidelines for optical resonator biochemical sensors," J. Opt. Soc. Am. B **26**(5), 1032–1041 (2009).
40. T. Yoshie, L. Tang, and S.-Y. Su, "Optical microcavity: Sensing down to single molecules and atoms," Sensors **11**(2), 1972–1991 (2011).
41. E. Luan, H. Shoman, D. Ratner, K. Cheung, and L. Chrostowski, "Silicon photonic biosensors using label-free detection," Sensors **18**(10), 3519 (2018).
42. J. E. Saunders, C. Sanders, H. Chen, and H.-P. Loock, "Refractive indices of common solvents and solutions at 1550 nm," Appl. Opt. **55**(4), 947–953 (2016).
43. R. Peltomaa, B. Glahn-Martínez, E. Benito-Peña, and M. Moreno-Bondi, "Optical biosensors for label-free detection of small molecules," Sensors **18**(12), 4126 (2018).
44. H. Nguyen, J. Park, S. Kang, and M. Kim, "Surface plasmon resonance: a versatile technique for biosensor applications," Sensors **15**(5), 10481–10510 (2015).
45. S. Geschwindner, J. F. Carlsson, and W. Knecht, "Application of optical biosensors in small-molecule screening activities," Sensors **12**(4), 4311–4323 (2012).
46. O. Laitinen, V. Hytönen, H. Nordlund, and M. Kulomaa, "Genetically engineered avidins and streptavidins," Cell. Mol. Life Sci. **63**(24), 2992–3017 (2006).
47. D. Frenzel and D. Willbold, "Kinetic titration series with biolayer interferometry," PLoS One **9**(9), e106882 (2014).
48. R. Karlsson, P. S. Katsamba, H. Nordin, E. Pol, and D. G. Myszka, "Analyzing a kinetic titration series using affinity biosensors," Anal. Biochem. **349**(1), 136–147 (2006).
49. B. Bhushan, D. R. Tokachichu, M. T. Keener, and S. C. Lee, "Morphology and adhesion of biomolecules on silicon based surfaces," Acta Biomater. **1**(3), 327–341 (2005).
50. Y. Guo, J. Y. Ye, C. Divin, B. Huang, T. P. Thomas, J. R. Baker Jr, and T. B. Norris, "Real-time biomolecular binding detection using a sensitive photonic crystal biosensor," Anal. Chem. **82**(12), 5211–5218 (2010).
51. M. J. Swann, L. L. Peel, S. Carrington, and N. J. Freeman, "Dual-polarization interferometry: an analytical technique to measure changes in protein structure in real time, to determine the stoichiometry of binding events, and to differentiate between specific and nonspecific interactions," Anal. Biochem. **329**(2), 190–198 (2004).
52. T. Arai, P. Kumar, C. Rockstuhl, K. Awazu, and J. Tominaga, "An optical biosensor based on localized surface plasmon resonance of silver nanostructured films," J. Opt. A: Pure Appl. Opt. **9**(7), 699–703 (2007).
53. D. E. Hyre, I. Le Trong, E. A. Merritt, J. F. Eccleston, N. M. Green, R. E. Stenkamp, and P. S. Stayton, "Cooperative hydrogen bond interactions in the streptavidin–biotin system," Protein Sci. **15**(3), 459–467 (2006).
54. R. F. Delgadillo, T. C. Mueser, K. Zaleta-Rivera, K. A. Carnes, J. González-Valdez, and L. J. Parkhurst, "Detailed characterization of the solution kinetics and thermodynamics of biotin, biocytin and haba binding to avidin and streptavidin," PLoS One **14**(2), e0204194 (2019).
55. X. Chen, L. Zhang, and D. Cui, "Surface plasmon resonance immunoassay for biotin determination on a home-made instrument," Procedia Technol. **27**, 87–88 (2017).